

Long term instability growth of radiatively driven thin planar shells*

R. J. Mason,^{†,a)} D. E. Hollowell, G. T. Schappert, and S. H. Batha
Los Alamos National Laboratory, Los Alamos, New Mexico 87545

(Received 24 October 2000; accepted 21 December 2000)

The Rayleigh–Taylor instability of radiatively driven thin copper foils is studied under pure ablation, as well as with beryllium buffers to provide additional pressure drive, in support of the target design for Inertial Confinement Fusion. Modeling was done with the RAGE adaptive mesh refinement code [R. M. Baltrusaitis, M. L. Gittings, R. P. Weaver, R. F. Benjamin, and J. M. Budzinski, *Phys. Fluids* **8**, 2471 (1996)] of experiments done on the OMEGA [T. R. Boehly, D. L. Brown, R. S. Craxton *et al.*, *Opt. Commun.* **133**, 495 (1997)] laser. The copper foils were typically 11.5 μm thick with 0.45 μm amplitude and 45 μm wavelength cosine surface perturbations. The beryllium layer was 5 μm thick. The drive was a “PS26”-like [J. D. Lindl, *Phys. Plasmas* **2**, 3933 (1995)] laser pulse delivering peak 160–185 eV radiation temperatures. Good agreement between experiment and simulation has been obtained out to 4.5 ns. Mechanisms for late time agreement are discussed. © 2001 American Institute of Physics. [DOI: 10.1063/1.1354150]

I. INTRODUCTION

Whenever a lower-density fluid is made to push on a higher-density fluid, there is a growth of perturbations on the surface at the density interface due to Rayleigh–Taylor (R–T) instability.^{1,2} The radiation in laser-driven hohlraums can be used to drive such an instability.³ With currently available laser energies, typically 20 kJ, this instability, at the high-density interfaces provided by metals in air, can only be studied in the motion of thin foils. Radiative ablation drives low-density ejected gas that accelerates such foils.^{4,5} In recent years such ablative Rayleigh–Taylor instability has been sedulously scrutinized for an Inertial Confinement Fusion (ICF) application.^{6,7} Low-density plastic foam buffers^{8–10} have been shown to stabilize the imprinting of laser perturbations on irradiation foils, which can be more beneficial than their material pressure enhancement of the RT instability of perturbations already in the foil.

Conversely here, we are interested in destabilizing effects from the *additional push* that can come from the presence of a lower-density buffer layer¹¹ on the drive side of the foils abutting the initial surface perturbations. Such layers have been included as beryllium ablators¹² in ICF capsule designs that ignite in one-dimensional calculations. Here, however, the extra material pressure from such buffers is shown to increase the acceleration of foils, and hasten their breakup from R–T instability. We seek to characterize such a breakup, both for its ICF implications and for its use in validating computer models that guide ICF design. We have conducted experiments at the Lawrence Livermore National Laboratory on NOVA,¹³ but principally on the OMEGA¹⁴ laser at the Laboratory for Laser Energetics (LLE) in Rochester. Both sets of experiments displayed this increased instability. Detailed modeling with LASNEX¹⁵ and with Los

Alamos National Laboratory’s RAGE¹⁶ adaptive mesh refinement (AMR) code has elucidated these results.

Our experiments have focused on planar shell targets that are substantially thinner than the perturbation wavelength. We have studied the contrasting dynamics obtained with just simple ablative drive, and then with the addition of material pressure drive. We anticipated and observed greater foil acceleration, and faster Rayleigh–Taylor (R–T) growth with the extra material pressure. We have focused on high- Z shells to see R–T effects associated with high density in the hydrodynamics and high opacity in the radiation transport. Available laser energy limited us to copper.

In what follows, we first describe the laser targets used and the experiments measuring target instability. We discuss one-dimensional simulations that show advancing radiation profiles and the resultant driven dynamics of thin copper foils. We next examine the effects of a thin beryllium buffer layer that is used to filter the radiative drive. We then show that the net drive is calculated to increase when this layer abuts the foils. We discuss the two-dimensional calculations used to track R–T instability growth. Electron thermal conductivity is found to provide important density profile smoothing. Mesh refinement tracks the evolving density details. Finally, in comparing the experiment and the simulation, we find generally good agreement during an early non-linear regime, during which R–T spikes grow to ~ 20 times the initial disturbance amplitude. We conclude with a survey of various adjustments that can be applied to the simulations to produce a good match to our experimental data at later times.

II. EXPERIMENTAL BACKGROUND

Our experiment compared two types of targets. One was filtered and buffered by a beryllium layer, while the other was only filtered. Figure 1 shows schematics of our two target classes. We used 5 μm of beryllium in each case to provide a constant filtering of the radiation reaching the cop-

*Paper G13 6, *Bull. Am. Phys. Soc.* **45**, 123 (2000).

[†]Invited speaker.

^{a)}Electronic mail: mason@lanl.gov

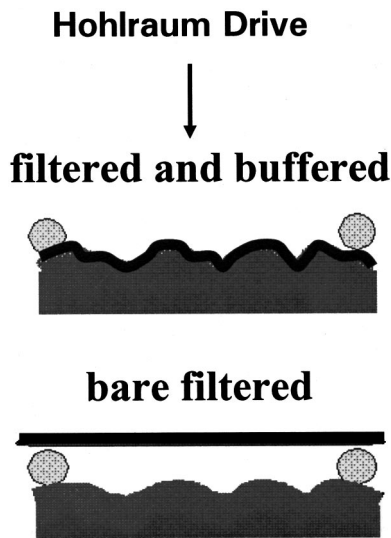


FIG. 1. Buffered and filtered (top), and bare filtered targets.

per. For the pure ablative drive the beryllium was set as a flat slab spaced $200\ \mu\text{m}$ beyond the $11.5\ \mu\text{m}$ copper foil. For the pressure drive the beryllium was contoured onto the perturbed surface of our foils and was in close contact. For our present studies the initial perturbation of the copper surfaces was a single mode, $0.45\ \mu\text{m}$ in amplitude with a $45\ \mu\text{m}$ wavelength.

At LLE, 45 beams of the OMEGA laser irradiated 1.4 mm radius tetrahedral hohlraums. Each beam typically delivered 400 J of $3\ \omega$, $0.35\ \mu\text{m}$ light for a total of 18 kJ in a “PS26” pulse. This produced a peak radiation temperature of $\sim 170\ \text{eV}$ in the hohlraum, as measured by the Dante diagnostic. Twelve additional beams delivering up to 4.4 kJ were reserved for driving the backlighter for face-on radiography. These beams impinged on a 0.5 mil iron disk producing the 6.7 keV Fe He_α line radiation for imaging the target, as shown in Fig. 2. The backlighter beams were time staggered in two groups to radiograph the package during the period of interest. The high x-ray energy was needed for penetrating the copper target and was known to be reliably achievable. Ultimately, we found that a higher energy would have been advantageous. In all cases, the copper foil in our R–T packages was positioned with spacers $200\ \mu\text{m}$ from the opening in the hohlraum wall, and viewed the interior of the hohlraum through a small slot. The XRFC camera records 16 pinhole images, four on each of its four strips. The timing of the individual strips is also staggered to follow the temporal

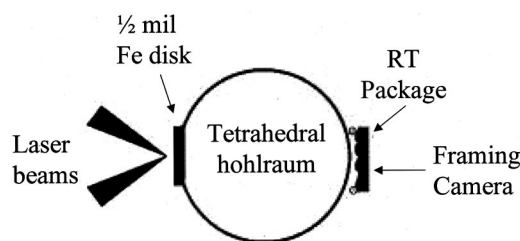


FIG. 2. Schematic of OMEGA experiment.

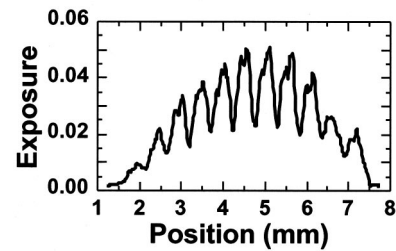
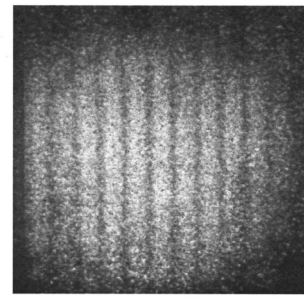


FIG. 3. The x-ray backlighter image and corresponding exposure of the growing perturbations. Fine structure is evident in the spike peaks.

development of the package. Because of the backlighter pulse-length considerations this period is typically 1.5–2.0 ns. The image timing separation on a given strip cannot be controlled and is typically about 60 ps. A typical radiograph image from a strip is shown in Fig. 3. One sees at least nine $45\ \mu\text{m}$ cycles of the growth from the initial $0.45\ \mu\text{m}$ amplitude sinusoidal perturbation.

The analysis of such images proceeds as follows. The image is digitized. A multiline lineout transverse to the corrugations records the signal on the backlighter profile. A multiline lineout along the corrugation direction records the noise, which shows no three-dimensional (3-D) deviations, i.e., none of the transverse periodicity. The signal is deconvolved with the MTF (Modulation Transfer Function) of the imaging system,^{17,18} using the measured noise with a standard Wiener filter technique.¹⁹ Then the backlighter spatial profile is removed by smoothing the logarithm of the deconvolved lineout over the period of the fundamental corrugation. This leaves the log of the backlighter profile, which can then be subtracted out, resulting in the perturbation growth pattern impressed on the backlighter profile. Since this pattern reflects the transmission through the copper structure, the logarithm represents the effective depth of copper penetrated by the x rays. Now Fourier analysis can be used to obtain the growth of the initial sinusoidal perturbation and subsequent harmonics in terms of the copper opacity integrated through the package. The material does not get hot enough to affect significantly the copper opacity for 6.7 keV x rays. Hence, the *equivalent cold copper amplitudes* of the perturbations are obtained by dividing by the cold copper opacity and density ($80\ \text{cm}^2/\text{g}$ at 6.7 keV, and $8.93\ \text{g}/\text{cm}^3$, respectively).

Even after this procedure the data is still fairly noisy. Since we have several shots (4 bare but filtered, and 3 buffered), we can bin the data from different shots into 200 ps time bins and average (bin-averaged), or average over the

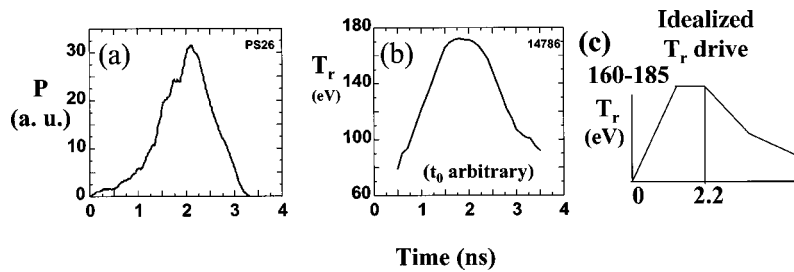


FIG. 4. (a) Laser pulse shape; (b) resultant radiative drive history; (c) LASNEX and RAGE input radiation temperature history.

images on an XRFC strip (strip-averaged). In either case, little growth occurs during a 200 ps interval. Typical exposures, as in Fig. 3, show fine scale grooves in the highest exposure points, corresponding to possible spikes in the center of the growing R–T bubbles.

A shaped laser pulse (“PS26”) accelerated the foil and drove the instability, Fig. 4(a). We typically recorded a radiative drive temperature history, Fig. 4(b), peaking at about 160–185 eV. Here, $t=0$ is somewhat arbitrary, but the drive is above 100 eV for about 2 ns. We idealized this as the radiation temperature T_r boundary condition of Fig. 4(c) for use in our LASNEX and RAGE calculations.

III. SIMULATIONS

A. 1-D LASNEX calculations

Early scoping calculations for this experiment were first performed with LASNEX. For the bare copper foils these calculations showed, for example, the results of Fig. 5. For a peak radiation temperature of 160 eV, the “PS26” pulse gives a 40 eV value in the drive region at 1 ns, rises to 85 eV by 4 ns, is near its peak at 2 ns, and then starts to push the foil to the left in the figure. The foil resides initially at $x=0$. By 6 ns its peak density point has moved to $x \sim -170 \mu\text{m}$. The peak Cu density goes to 16 g/cm^3 at 2 ns, drops back to 7.5 g/cm^3 by 3 ns, and to only 4 g/cm^3 by 6 ns. At this late time the drive just ahead of the density peak is down to only 40 eV.

In one dimension we calculated mass trajectories that matched side-on radiography measurements conducted at NOVA. For OMEGA typical zonal $x-t$ plots for bare Cu foils are given in Fig. 6. The radiation is first absorbed by the Be layer, which here serves only as a filter. This filter initially resides $200 \mu\text{m}$ in front of the foil, separated from the

foil by the spacers of Fig. 1(b). It explodes, with its outer regions moving toward the driving radiation and reaching $600 \mu\text{m}$ by 1.9 ns. The filter’s mass heads toward the copper foil, striking its expanding outer regions by about 700 ps. After 1 ns roughly the entire filter mass is blowing toward the driver. The ablating Cu mass reaches $x \sim 400 \mu\text{m}$ by 6 ns, while copper zones clustering near the density peak are pushed back to $x \sim -350 \mu\text{m}$ by 10 ns.

If the filter is placed at $200 \mu\text{m}$ or beyond, its presence has little hydrodynamic effect on the peak density trajectory for the Cu foil. When, for example, we initiated it at $2000 \mu\text{m}$, the resultant density trajectory was the same. The filter does, however, weaken the drive, retarding its arrival at the copper. We can see this from Fig. 7(a). At 1 ns, when the drive is at 100 eV in the hohlraum, it is still only 60 eV adjacent to the foil. However, by 1.3 ns the radiation temperature profile T_r is nearly flat across the filter. Trajectories of the foil peak densities show that with remote Be filtering the foils move most slowly, due to the delay in the drive at the foil. In unfiltered light the copper foils move about $25 \mu\text{m}$ farther by 6 ns. This is shown in Fig. 7(b). Finally, with the Be attached to the foil to provide additional pressure as a buffer layer, the copper moves the farthest distance—to a point $\sim 50 \mu\text{m}$ ahead of the bare filtered foil by 6 ns. We retained the beryllium filter in the bare copper experiments to ensure a similar drive on the copper with and without buffering.

More general parameter studies confirmed that, for optimum pressure acceleration, the beryllium layer should initially touch the copper. The beryllium layer is largely penetrated by the radiation at 1 ns. Figure 8 compares at 1 ns the density ρ and radiative temperature, T_r , profiles for a remote Be layer versus an attached Be buffer layer. In each case, the

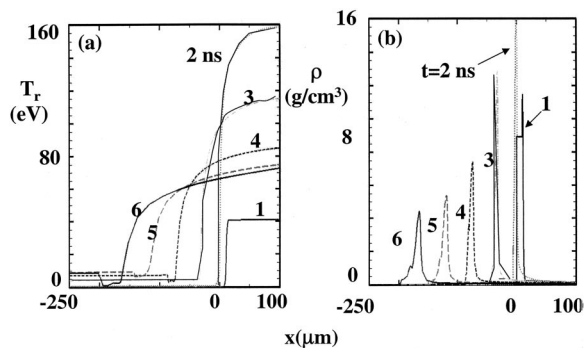


FIG. 5. One-dimensional evolution of filtered bare copper foils. (a) Radiation temperature, T_r history; (b) evolving densities.

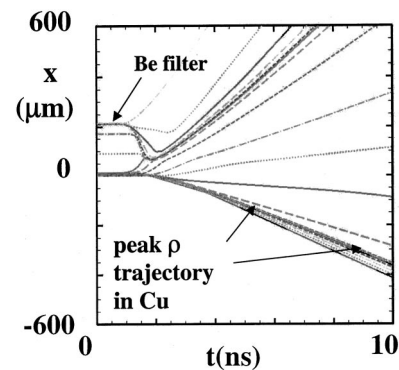


FIG. 6. (a) The $x-t$ history of the Langrangian zone boundaries; radiation delivered from above.

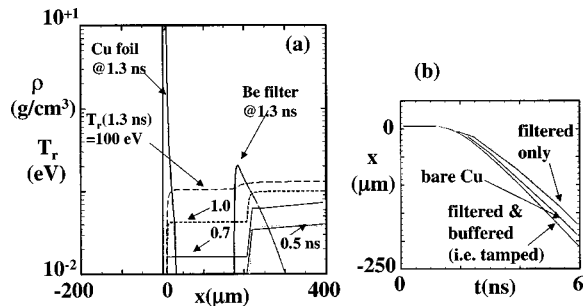


FIG. 7. (a) The demonstrated delay in the radiative drive near the foil due to the presence of a Be filter. (b) Trajectories of the peak density points for (i) filtered bare, (ii) unfiltered bare, and (iii) buffered Cu foils. The filtered bare foil is the slowest.

T_r reaches 65 eV in the densest regions ($\rho \geq 3$ g/cm³) of the Cu, but the copper density is shocked only 1.3-fold in the bare case. In the buffered case, the beryllium layer is seen still abutting the foil, and the shock exhibits a 3.1-fold increase in density. Additional studies, in which the beryllium mass was kept constant, but with its initial density artificially reduced, showed that the greatest drive came at natural, solid density. When, for example, they beryllium was treated computationally as a 0.1 g/cm³ density foam, the peak shock density in the copper at 2 ns was 25% lower than with a solid Be buffer, indicating a weaker shocking of the copper by the same drive. Consequently, we avoided the use of foams in our experiments.

B. 2-D RAGE results

For two-dimensional calculations we found that the LASNEX mesh tangled seriously just as important nonlinear features in the R-T growth were emerging; therefore, we turned to RAGE. This Eulerian model treats the interfaces between the copper, beryllium, and background void and regions of steep density and temperature variation with adaptive mesh refinement. The largest cells in our calculations—generally in the void—were 1.125 μm square. Our smallest cells—mostly those near the interfaces—were three levels higher in refinement, i.e., 0.1406 μm on a side. This gave us 320 cells laterally to resolve the initial 45 μm perturbation, and 8.6 cells to resolve the 9 μm peak-to-valley amplitude

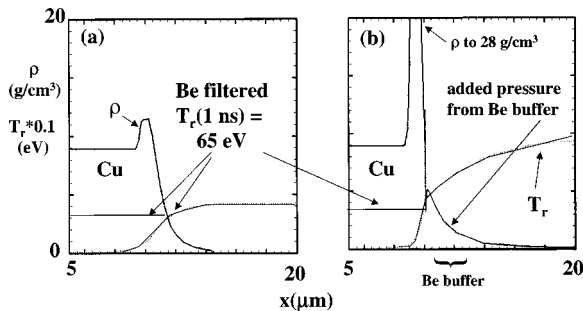


FIG. 8. Density and T_r profiles at 1 ns for (a) the bare filtered Cu foil, and (b) the Be-buffered foil—with buffering a layer of Be is still “leaning” up against the Cu to give it the additional push that leads to the stronger shock.

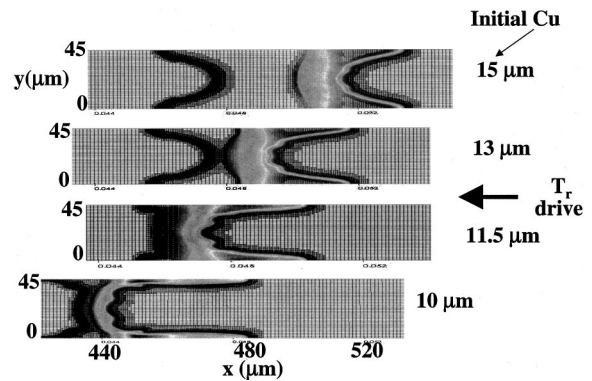


FIG. 9. A sequence of accelerated bare foils of varied initial thickness.

perturbations. To avoid singularities in the Eulerian calculations, the void was actually treated as low density, 10^{-3} g/cm³, air.

For all the calculations reported here the radiative drive was supplied as a temperature boundary condition on the right at the 1200 μm position along the x axis. The buffer layer had a cosine profile on both sides, being an equal 5 μm thick at all the vertical (y) positions. Our initial runs were made with radiation transport “on,” but electron thermal conduction “off.” The rapid development of fine-scale density filaments or “filigree” plagues the results of these runs. This appeared on the drive side of the copper or beryllium. The source of the effect is purely hydrodynamic and persists when the radiation transport is suppressed and the foils are accelerated by an equivalent push from high-pressure air.

The RAGE mesh has difficulty representing a smooth cosine surface profile on the background Cartesian mesh. The steep density gradients at the copper interface with air or beryllium introduces stair-stepped density contours following the edges of the square mesh elements. The density steps serve as short-wavelength seeds for instability. Even with AMR, the smallest cells must be crossed diagonally by the surface interface, with mass fractions apportioned on either side. In a mixed cell the smallest fraction of copper permitted, for example, is $(1/2^n)^2$. We started with $n=2$ and found some reduction in the short-wavelength seeding when we increased n to 8. The seeding could be further reduced when we terraced the interface between the copper and the air or beryllium by introducing one row of cells set at one third solid copper density. The initial density drop then occurred over three cells rather than two. This is a somewhat cumbersome manual procedure, however, We achieved the greatest smoothing by simply turning on the electron thermal transport in RAGE. In our experiment thermal conductivity delivers heat to the micro-size filaments and fire polishes them away.

First, when we examined a calculated sequence of bare filtered foils under the same “PS26” drive, with initial thickness ranging from 15 down to 10 μm , and all at 5.6 ns, we found properly, that the thinner, fastest moving foils developed the longest spikes, as in Fig. 9, helping us to “tune” our experiments. Note that the adaptive mesh refinement allows for high resolution at the material interfaces. We see that the 11.5 μm foil has developed spikes ~ 30 μm long.

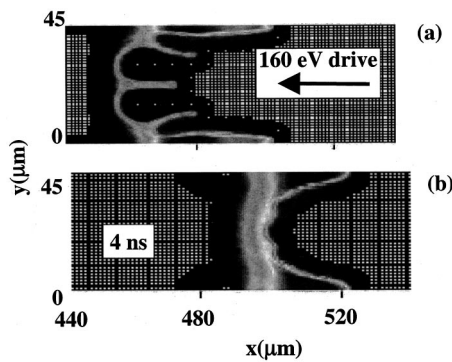


FIG. 10. The buffered foil (a) shows greater acceleration at 4 ns and the development of a strong central density feature; (b) is the bare foil.

We shall see that this presents a problem for our experimental diagnostics.

Comparing our calculations employing electron thermal conductivity for the buffered and bare foil accelerations, we find that the pressure from the beryllium buffer does, indeed, provide an extra push to the copper foil. The two foils start at the $x=600 \mu\text{m}$ position in Figs. 10(a) and 10(b). The figure illustrates that in response to a 160 eV peak drive temperature the buffering drives the center of the copper foil $50 \mu\text{m}$ farther to the left by 4 ns. The buffered foil develops a strong central filament in the R–T bubble, and side fingers indicative of increased second and fourth harmonic growth. Both targets show the development of spikes adjacent to the walls exceeding $30 \mu\text{m}$ in length. Figures 11(a) and 11(b) show the modal growth with time of the disturbed amplitude, as calculated with RAGE; only the first and second harmonics are plotted. We post-processed the code output to obtain values of $\rho R = \int \rho(x, y) dx$ at 40 lateral positions y . The ρR contributions from any initial beryllium and the vacuum (low-density air) were subtracted away. The result was then divided by the initial copper density to determine a foil thickness at the various lateral positions, $\tau(y)$. This was Fourier analyzed to yield the modal amplitudes. At 4 ns the first four modal amplitudes in the buffered case (b) are 6.6, 4.0, 2.4, and $1.0 \mu\text{m}$, summing to $14.0 \mu\text{m}$. Higher-order modes (to about the tenth) sum to another $6 \mu\text{m}$ and are needed to produce the large spikes, top and bottom.

IV. COMPARISON OF EXPERIMENTS AND CALCULATIONS

We also compare our data from the OMEGA experiments with our RAGE predictions in Fig. 11. Each data point is a strip average, as discussed with Fig. 3. The predicted first-order perturbations (determined as above) start at $0.45 \mu\text{m}$ and grow beyond $6 \mu\text{m}$ in equivalent amplitude (effective length) by 6 ns. Our calculations for the first and second harmonic growth are in good agreement with the data until about 4.5 ns for the bare copper, and to 4.0 ns for the buffered copper foil, when the data appears to saturate.

As a probable explanation for this discrepancy, we noted that our observation of the backlighter was not truly face-on but was instead, typically, up to 4° to the side due to parallax of the framing camera geometry. This would lead to a re-

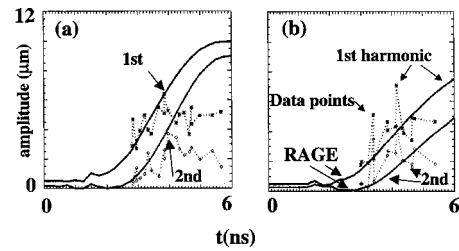


FIG. 11. Perturbation growth in the buffered foil (a) is greater than with the bare foil (b). Agreement of the RAGE calculations with data is good at early times.

duced ρR measurement, as we looked slightly across a spike instead of straight down its extent. Simulations of this effect in buffered foils showed, however, that as much as an unrealistic 20° observation angle would be needed to reduce the calculated first harmonic amplitude from $\sim 9 \mu\text{m}$ to the observed $5 \mu\text{m}$ at 5.5 ns.

Second, it is likely that the effective temperature driving the foils was lower than that measured in the hohlraums at late time, by virtue of energy loss at the edges of the foil package as it lifted off the hohlraum wall. The spacers (Fig. 1) holding the package allowed for some leakage, even at $t=0$. We crudely modeled this effect by truncating the radiative drive after 2.2 ns, when the copper was calculated to move off the hohlraum through its initial $11 \mu\text{m}$ thickness. We found that this could bring the buffered data and simulation into better accord for both the first and second harmonics. However, the unbuffered data are better matched without truncation, possibly because it separates from the hohlraum more slowly.

Finally and most significantly, we consider that for sufficiently long spikes the transmitted backlighter signal is in the noise of the detector. The opacity of Cu is a nearly constant $K_r=80 \text{ cm}^2/\text{g}$ (from the SESAME tables appropriate to 50–120 eV material temperatures, the observed Cu shell densities, and for the 6.7 keV iron irradiation). Let $\tau(y)$ be the equivalent cold copper thickness of the foil at a distance y transverse to the corrugations, $\tau_e(y)$ an effective thickness, I_0 the initial backlighter intensity, and N the noise signal, respectively. The observed signal in the foil radiograph then becomes, $I = I_0 \exp[-\rho K_r \tau(y)] + N = I_0 \exp[-\rho K_r \tau_e(y)]$. Should the true copper thickness in a spike become extremely large, $\tau(y) \rightarrow \infty$, the radiograph will still register $I=N$, equivalent to a maximal effective thickness, $\tau_e(y) \rightarrow -(1/\rho K_r) \log\{N/I_0\} = -14.0 \log\{N/I_0\} \mu\text{m}$. If we can measure down to level $N/I_0=0.15$, i.e., 15%, of the initial intensity, we would record spikes of maximal length, $\tau_e = 26.0 \mu\text{m}$. This effect cannot be deconvolved from the data, but we can apply it to the simulations.

Figure 12 shows the RAGE predictions adjusted for such possible minimal sensitivities N/I_0 ranging from 20% down to 10%. Here, we Fourier analyzed the effective thickness τ_e , extracted the first and second harmonics, and plotted them with the corresponding experimental data. We see that the first harmonic data is best matched for a minimum sensitivity between 15% and 20%. The second harmonic is still only matched out to 4.5 ns.

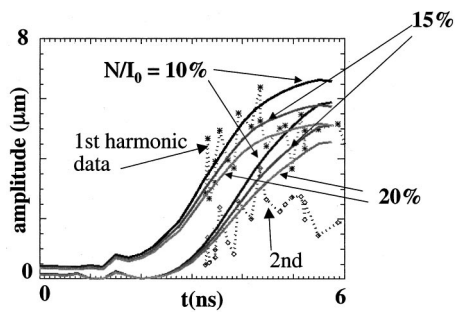


FIG. 12. The first and second modal amplitudes are plotted for both the data and the adjusted RAGE predictions. The RAGE amplitudes versus time are plotted for an effective thickness $t_e(y)$, assuming noise levels $N/I_0=0.1$, 0.15, and 0.2.

As an alternative, a reasonable match to the data is obtained by simply applying a 20 μm effective copper depth ceiling on the RAGE calculation before Fourier analyzing the result. The buffered case with strip-averaged data is shown in Fig. 13(a). For all measured times this yielded good agreement of our first harmonic calculations with data for the bare and the buffered foils. The calculated second harmonic is also in good agreement with the bare target data, but still too high for the buffered case. For Fig. 13(b) we used the same 20 μm ceiling but plot the time-binned-averaged data. This gives a much more detailed agreement with the data, for the first harmonic, except for one outlier for 3.9 ns. Last, in Fig. 13(c) we compare strip-averaged data from the buffered targets to our calculated results with the 20 μm ceiling at a higher 185 eV peak drive temperature. Here, the calculated modal growth is faster, so that the ceiling on total amplitudes is encountered sooner, resulting in less agreement with the first harmonic data and better second harmonic agreement beyond 4 ns.

V. CONCLUSION

LASNEX modeling has provided a good picture of the effects of radiative filtering by our beryllium layer. Two-dimensional modeling with RAGE provided smooth results in accord with measurements when adjustments were made for instrumental limitations. In both experiment and simulation, due to the additional material backpressure, the Be-buffered foils showed enhanced acceleration and increased instability over bare ablating foils. This could be a concern for ICF

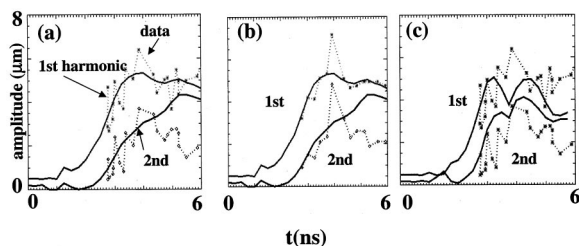


FIG. 13. A comparison of (a) strip-averaged data, and (b) time-binned data calculations, and (c) the strip-averaged comparison for a higher, 185 eV peak hohlraum temperature.

design applications. It provides useful validation for our emerging RAGE model. In our simulation of modal growth, amplitude reductions from backlighting at an angle prove to be minimal, and the effects of moderate variations in the peak hohlraum temperature are inconclusive. Finally, the measured spike growth amplitudes appear to saturate due to the range-related loss of the probing backlighter illumination. Good numerical agreement with our first harmonic measurements is achieved, assuming a loss of the backlighter transmission beyond 20–26 μm of copper, corresponding to strongly diminished instrument sensitivity at 20%–15% of the initial backlighter intensity. Examination of the second harmonic and higher harmonic data warrants further scrutiny.

ACKNOWLEDGMENTS

We gratefully acknowledge the efforts of N. Hoffman, M. Gittings, and R. Weaver and the LASNEX and RAGE teams in enabling the code simulations. We thank R. E. Turner of LLNL for analysis of the Dante hohlraum temperature data.

This work was performed under the auspices of the U.S. Department of Energy by the Los Alamos National Laboratory under Contract No. W-7405-ENG-36.

¹G. Taylor, Proc. R. Soc. London, Ser. A **201**, 192 (1950).

²S. Chandrasekhar, *Hydrodynamic and Hydromagnetic Stability* (Dover, New York, 1961).

³E. G. Gamaly, *Nuclear Fusion by Inertial Confinement* (CRC Press, Boca Raton, 1993).

⁴K. Budil, M. Edwards, B. Lasinski, B. Remington, L. Sutter, A. Wan, and P. Stry, Bull. Am. Phys. Soc. **44**, 57 (1999).

⁵K. S. Budil, B. A. Remington, T. A. Peyser, K. O. Mikaelian, P. L. Miller, N. C. Woolsey, W. M. Wood-Vasey, and A. M. Rubenchik, Phys. Rev. Lett. **76**, 4536 (1996).

⁶B. A. Remington, S. V. Weber, M. M. Marinak, S. W. Haan, J. D. Kilkenny, R. J. Wallace, and G. Dimonte, Phys. Plasmas **2**, 241 (1995).

⁷H. Takabe, H. Nagatomo, A. Sunahara, N. Ohnishi, A. Mahdy, Y. Yoda, S. Naruo, H. Azechi, H. Nishimura, and K. Mima, Plasma Phys. Controlled Fusion **41**, A75 (1999).

⁸R. J. Mason, R. A. Kopp, H. X. Vu, D. C. Wilson, S. R. Goldman, R. G. Watt, M. Dunne, and O. Willi, Phys. Plasmas **5**, 211 (1998).

⁹R. G. Watt, R. J. Mason, J. Duke *et al.*, Phys. Rev. Lett. **81**, 4644 (1998).

¹⁰R. J. Mason, R. A. Kopp, H. X. Vu, D. C. Wilson, S. R. Goldman, R. G. Watt, and O. Willi, *Laser Interaction and Related Phenomena*, 13th Conference, AIP Conference Proceedings **406**, edited by G. H. Miley and E. M. Campbell, 1997, p. 140.

¹¹R. Mason, D. Hollowell, G. Schappert, and S. Batha, Bull. Am. Phys. Soc. **44**, 57 (1999).

¹²D. C. Wilson, P. A. Bradley, S. R. Goldman, N. M. Hoffman, R. W. Margevicius, R. B. Stephens, and R. E. Olsen, Fusion Technol. **38**, 16 (2000).

¹³E. M. Campbell, J. T. Hunt, E. S. Bliss *et al.*, Rev. Sci. Instrum. **57**, 2101 (1986).

¹⁴T. R. Boehly, D. L. Brown, R. S. Craxton *et al.*, Opt. Commun. **133**, 495 (1997).

¹⁵G. B. Zimmerman and W. L. Kruer, Comments Plasma Phys. Control. Fusion **2**, 51 (1975).

¹⁶R. M. Baltrusaitis, M. L. Gittings, R. P. Weaver, R. F. Benjamin, and J. M. Budzinski, Phys. Fluids **8**, 2471 (1996).

¹⁷H. F. Robey, K. S. Budil, and B. A. Remington, Rev. Sci. Instrum. **68**, 792 (1997).

¹⁸V. A. Smalyuk, T. R. Boehly, D. K. Bradley, J. P. Knauer, and D. D. Meyerhofer, Rev. Sci. Instrum. **70**, 647 (1999).

¹⁹W. H. Press, S. A. Teukolsky, W. T. Vetterlig, and B. P. Flannery, *Numerical Recipes in FORTRAN*, 2nd ed. (Cambridge University Press, Cambridge, 1992), p. 539.